Mechanics Research Communications 122 (2022) 103889

Contents lists available at ScienceDirect

Mechanics Research Communications

journal homepage: www.elsevier.com/locate/mechrescom

Bandgap merging with double-negative metabeam

Ankur Dwivedi [a,*], Arnab Banerjee [b], Sondipon Adhikari [c], Bishakh Bhattacharya [a]

[a] Department of Mechanical Engineering, Indian Institute of Technology Kanpur, Kanpur, India
[b] Department of Civil Engineering, Indian Institute of Technology Delhi, New Delhi, 110016, India
[c] James Watt School of Engineering, University of Glasgow, Glasgow, UK

ARTICLE INFO

Keywords:
Metabeam
Negative mass
Negative stiffness
Double negative metabeam
Metamaterials
Metastructures
Bloch–Floquet theorem
Bandgap merging
Locally resonant bandgaps

ABSTRACT

We theoretically investigate the bandgap formation in an Euler–Bernoulli beam-based metastructure with periodically attached double negative 3-dof local resonators. The idiosyncratic physical phenomena found in mechanical metamaterials, such as negative stiffness and mass, are introduced in the attached local resonator to design the double negative metabeam. The transfer matrix method with the Bloch–Floquet formulation is implemented in a unit cell of the double negative metabeam. The complex band structure describes the existence of various locally resonant attenuation bandgaps on the frequency spectrum. Further system analysis is conducted to illustrate the merging of the negative stiffness and mass controlled locally resonant bandgaps. A significant increase of 164% is found in the attenuation bandwidth due to the merging of locally resonant bandgaps.

1. Introduction

The dynamics of the elastic beam with attached local resonators has engrossed researchers from the decades for controlling the vibration in structures [1–5]. Here we propose a metabeam with periodically attached 3-dof special double negative resonating unit to the host structure having a spring–mass system with specified boundary conditions. The stiffness and mass of the attached resonators to the host beam modulate the wave propagation in the system. Due to the frequency-dependent wave propagation properties, mapping the excitation frequency with the wavenumber exhibits various locally resonant attenuation bands on the frequency spectrum. Analysis of the isolated single unit cell from the metabeam gives wave propagation characteristics in the designed metastructure. The specified boundary conditions for a single unit cell in conjunction with the transfer matrix method application give the correlation between the state vectors of either side. The logarithm of the eigenvalues of the transfer matrix gives the wavenumber for the metabeam [6]. Propagation and attenuation characteristics of a wave are dependent on the numerical values of the wavenumber, which can be purely real or imaginary and complex [7]. According to the bandgap formation mechanism, the attenuation bands can be categorized as locally resonant and Bragg's Scattering bandgap. The locally resonant bandgaps are formed due to the simultaneous out-of-phase motion of multiple resonating units, making dynamic effective mass or effective stiffness of the structure negative in a specific band of the excitation frequency. Bragg's scattering bandgap is formed because of the destructive interference of the waves in the higher frequency region. These elastic metastructures can exhibit wideband vibration damping characteristics because of the locally resonant bandgaps. The application of these structures can also be extended for vibration energy harvesting [8,9]. The locally resonant bandgaps can be tuned on the frequency spectra with the help of the stiffness and mass of the resonators. An elastic beam with an attached spring–mass system exhibits a narrow locally resonant band. Many works are reported in the literature for widening the locally resonant bandgap [10–15]. In this direction, researchers also proposed multi-degree of freedom resonator attached to the elastic beam to study the multi flexural bandgaps. However, these studies may not produce wider bandgaps due to separation in different frequency ranges. The effect of eigenfrequencies apart from the individual natural frequency of resonators in the multi-degree of freedom system is also essential to communicate, which plays a vital role in forming the locally resonant bandgaps.

This article presents a special double negative resonator attached to the elastic beam to address the research gap in the literature. By incorporating the idiosyncratic physical properties like negative stiffness and mass of mechanical metamaterials [16–19] through the discrete spring–mass system, the double negative metabeam is designed. The bandgap formed due to the attached double negative resonators are tuned to merge with the help of derived critical physical system parameters. This analysis increases the efficacy of the designed metabeam for wideband

* Corresponding author.
E-mail addresses: ankurdwi@iitk.ac.in (A. Dwivedi), abanerjee@iitd.ac.in (A. Banerjee), Sondipon.Adhikari@glasgow.ac.uk (S. Adhikari), bishakh@iitk.ac.in (B. Bhattacharya).

https://doi.org/10.1016/j.mechrescom.2022.103889
Received 21 October 2021; Received in revised form 23 February 2022; Accepted 23 March 2022
Available online 6 April 2022

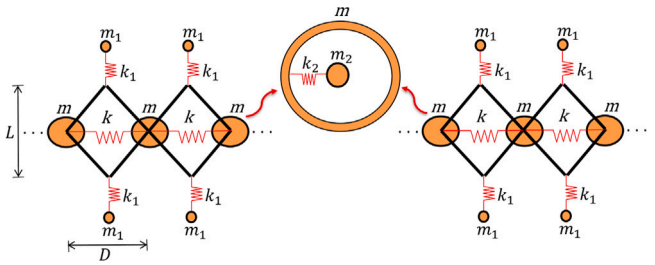

Fig. 1. Discrete double negative metamaterial having negative stiffness and mass characteristics. A series of primary masses m attached with spring having stiffness k by four rigid massless bars with secondary spring–mass systems (k_1 and m_1) attached to the diagonally opposite nodes. This system acts as a negative stiffness metamaterial. Further, inside the primary mass m, a resonating mass m_2 is present, making it a mass-in-mass system and acting as a negative mass metamaterial.

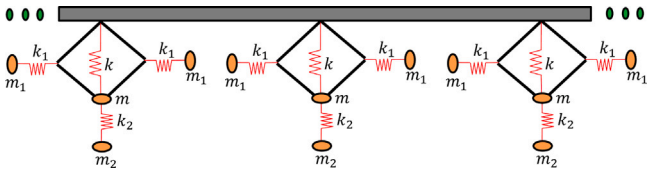

Fig. 2. Euler–Bernoulli based double negative metabeam. The local 3-dof resonator attached to the host beam is having negative stiffness and mass characteristics.

vibration control due to the merging of the various locally resonant attenuation bands along the frequency spectrum.

2. Double-negative metabeam

Fig. 1 shows double-negative mechanical metamaterial in the discrete form, previously investigated by Huang et al. [20]. This mechanical metamaterial lattice structure has primary masses m connected by spring having stiffness k. The secondary mass m_1 and spring having stiffness k_1 are attached to primary masses m with the help of four massless bars on either side with frictionless revolute joints such that nodes connecting the primary masses traverse only horizontally. This special structure is inspired by the Helmholtz resonator and called negative stiffness metamaterial [21–23]. To introduce double negativity in this system, primary mass m has a mass-in-mass structure. The internal resonating mass m_2 is connected to m with spring having stiffness k_2. The mass-in-mass structure of the primary mass m is called a negative mass metamaterial and can be represented as a single degree of freedom spring–mass system having negative mass [24,25]. Hence, the whole discrete spring–mass system is called a double-negative metamaterial.

As shown in Fig. 2, we propose a beam-based metastructure in which double negative resonators are attached periodically at uniform locations on an elastic beam. The beam assumed in the metastructure is Euler–Bernoulli beam. The massless bar structure with spring–mass systems (m_1, k_1) and (m, k) introduce dynamic negative stiffness in the horizontal direction. On the other side, the extended spring–mass systems (m_2, k_2) coupled with (m, k) becomes a mass-on-mass system and introduce dynamic negative mass effect in the vertical direction. Therefore, the entire 3-dof spring–mass resonator attached to the beam introduces a double negative effect in a specific excitation frequency band in the metabeam. Hence, the proposed metastructure with a 3-dof resonator attached to the beam may be expressed as a double negative metabeam.

The dynamics of negative stiffness [21,23,26] and negative mass resonator [24,25] is investigated thoroughly in the literature. The characteristic equations can be derived for the effective stiffness and mass for a unit cell of the metabeam with attached 3-dof resonators.

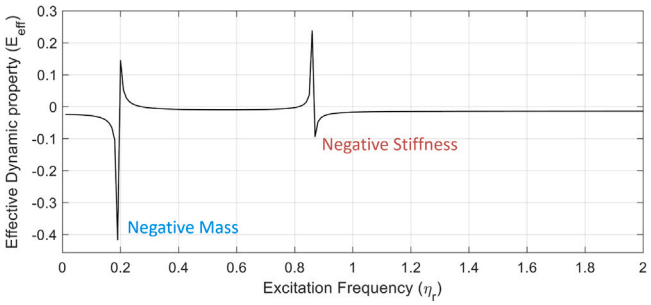

Fig. 3. The effective dynamic properties (mass and stiffness) of the metabeam are negative in a frequency range.

To find the effective stiffness and mass of the system, we need to find the effective force and momentum of the system, respectively. The effective dynamic properties (E_{eff}) of the system can be derived using the closed-form expressions of y_1 and y_2 given in Appendix A. Fig. 3 elucidates the variation of the effective dynamic property on the frequency scale. The effective stiffness and mass of the system are negative in a frequency range. Therefore, dynamic physical properties will modulate wave propagation inside the designed metabeam. The simultaneous out-of-the-phase motion of multiple resonating units make the effective physical properties (mass or stiffness) of the system frequency contingent due to the occurrence of local resonance phenomenon, resulting in the formation of locally resonant bandgaps. By changing the natural frequency (mass and stiffness) of resonators in the metastructure, edging frequencies of the bandgap can be changed. The following section explains the analytical formulation of the Euler–Bernoulli beam-based metabeam.

3. Analytical formulation

Equation of motion of the Euler–Bernoulli beam for free vibration can be written as

$$EI\frac{\partial^4 w(z,t)}{\partial z^4} + \rho A\frac{\partial^2 w(z,t)}{\partial t^2} = 0 \tag{1}$$

where EI is the flexural rigidity of the beam, ρ is the density of the material, and A is the cross-section area of the beam. w is the transverse deflection of the beam in $z-$direction, which is the function of the space (z) and time (t).

Eq. (1) can be non-dimensionalized by assuming $z = L_b\tilde{z}$, $t = \omega\tau$, $w(z,t) = W\tilde{w}(\tilde{z},\tau)$. Here L_b is length of the unit cell in metabeam, ω is the natural frequency of the beam. L_b, ω and W relate the respective dimensional terms to non-dimensional terms. Based on this, non-dimensional form of Euler–Bernoulli beam equation may be written as

$$\frac{\partial^4 \tilde{w}(\tilde{z},\tau)}{\partial \tilde{z}^4} + \frac{\partial^2 \tilde{w}(\tilde{z},\tau)}{\partial \tau^2} = 0 \tag{2}$$

where $\omega^2 = \frac{EI}{\rho A L_b^4}$. For solving Eq. (2), we assumed the displacement in the form $\tilde{w}(\tilde{z},\tau) = X(\tilde{z})e^{i\overline{\Omega}\tau}$, where $\overline{\Omega} = \frac{\varpi}{\omega}$ is the ratio of the temporal frequency of the wave to the natural frequency of the beam. After substituting the assumed displacement in Eq. (2), Euler–Bernoulli beam equation could be rewritten as

$$X^{IV}(\tilde{z}) - \overline{\Omega}^2 X(\tilde{z}) = 0 \tag{3}$$

The continuity equations for the n^{th} unit cell in the metabeam can be written for displacement, slope, moment, and shear force, respectively as in Eq. (4), where μ_f is the amplitude of the non-dimensionalized

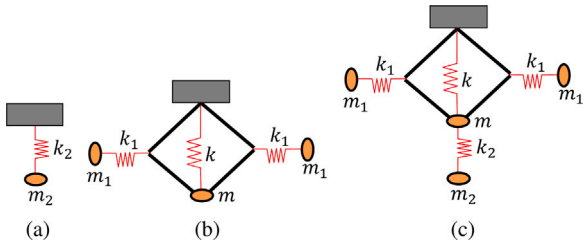

Fig. 4. (a) Negative mass resonator (b) Negative stiffness resonator (c) Double negative resonator.

shear force induced to the metabeam due to the attached 3-dof double-negative resonator.

$$\begin{aligned} X_n(0) &= X_{n-1}(1) \\ X_n'(0) &= X_{n-1}'(1) \\ X_n''(0) &= X_{n-1}''(1) \\ X_n'''(0) - \mu_f &= X_{n-1}'''(1) \end{aligned} \tag{4}$$

The mode shape function $X(\tilde{z})$ for obtaining the general solution to the Euler–Bernoulli beam can be written as in Eq. (5), where A, B, C, and D are unknown constants. The defined set of boundary conditions can find these constants. Substitution of the assumed solution from Eq. (5) in Eq. (3) yields the value of λ for the Euler–Bernoulli beam as $\lambda = \sqrt{\overline{\Omega}}$. It gives the relation between the spatial frequency ratio $\overline{\Omega}$ and eigenfrequency λ for the metabeam.

$$\begin{aligned} &X(\tilde{z}) = \\ &\begin{bmatrix} \cos(\lambda\tilde{z}) & \sin(\lambda\tilde{z}) & \cosh(\lambda\tilde{z}) & \sinh(\lambda\tilde{z}) \end{bmatrix} \\ &\times \underbrace{\begin{bmatrix} A & B & C & D \end{bmatrix}^T}_{Constants} \end{aligned} \tag{5}$$

Fig. 4 illustrates the development of various resonators in chronological order. The resonator shown in Fig. 4(a) is a simple, widely used single degree of freedom negative mass resonator. The conceptual design of negative stiffness resonator [23,27] is shown in Fig. 4(b). By combining these two resonators, the double negative resonator can be designed as depicted in Fig. 4(c). ω_1 ω_2 and ω_3 are the natural frequencies of the resonators for the spring–mass systems (m_1, k_1), (m_2, k_2) and (m, k), respectively. Therefore, ω_1 and ω_3 are associated with negative stiffness resonator and ω_2 belongs to the negative mass resonator. The non-dimensionalized natural frequencies Ω_1, Ω_2 and Ω_3 can be defined as $\Omega_1 = \frac{\omega_1}{\omega}$, $\Omega_2 = \frac{\omega_2}{\omega}$ and $\Omega_3 = \frac{\omega_3}{\omega}$, which are the ratio natural frequency of the resonators to natural frequency the beam.

To comprehend the dependency of the various critical physical parameters on the band structure, we can write ${\Omega_1}^2 = \frac{\mu_s}{\theta}$, ${\Omega_2}^2 = \frac{\mu_s \Theta_1 \kappa_2}{\theta \kappa_1}$ and ${\Omega_3}^2 = \frac{\mu_s \Theta_2}{\theta \kappa_1}$, where $\theta = \frac{m_1}{\rho A L_b}$, which is the ratio of mass of the resonator (m_1) to the beam and $\mu_s = \frac{k_1 {L_b}^3}{EI}$ is the stiffness ratio. Θ_1 and Θ_2 are the mass ratios, which are defined as $\Theta_1 = \frac{m_1}{m_2}$ and $\Theta_2 = \frac{m_1}{m}$. $\kappa_1 = \frac{k_1}{k}$ and $\kappa_2 = \frac{k_2}{k}$ are the stiffness ratios for the resonators. Additionally, the non-dimensionalized resonating frequencies $\eta_{r1} = \frac{\overline{\Omega}}{\Omega_1}$, $\eta_{r2} = \eta_{r1}\sqrt{\frac{\kappa_1}{\kappa_2 \Theta_1}}$ and $\eta_{r3} = \eta_{r1}\sqrt{\frac{\kappa_1}{\Theta_2}}$ can be defined as the ratio of the excitation frequency with natural frequencies of the resonators and can be reduced in terms of Θ_1, Θ_2, κ_1, κ_2 and η_{r1}. Hence, all the governing independent non-dimensional critical system parameters are η_{r1}, θ, Θ_1, Θ_2, κ_1, κ_2 and μ_s.

For finding the shear force due to the double-negative resonator on the beam, the free body analysis is done for the n^{th} 3-dof resonator along z direction in Appendix A. Hence, the non-dimensionalized shear force μ_f in the continuity equation can be written as

$$\begin{aligned} \mu_f &= \frac{\tilde{f}_n {L_b}^3}{WEI} = \mu_s \times \\ &\underbrace{\left[\frac{\alpha^2}{2}\frac{\overline{\Omega}^2}{{\Omega_1}^2 - \overline{\Omega}^2} - \frac{k}{k_1}\right]\left[1 - \frac{1}{1 - \frac{\left\{\kappa_2 \frac{\overline{\Omega}^2}{{\Omega_2}^2 - \overline{\Omega}^2} + \frac{\overline{\Omega}^2}{{\Omega_3}^2}\right\}}{\left\{1 - \kappa_1 \frac{\alpha^2}{2}\frac{\overline{\Omega}^2}{{\Omega_1}^2 - \overline{\Omega}^2}\right\}}}\right]}_{\chi} X_n(0) \\ &= \mu_s \chi X_n(0) = \vartheta X_n(0) \end{aligned} \tag{6}$$

where $\vartheta = \mu_s \chi$, $\alpha = \frac{L}{D}$ is the aspect ratio of the resonator. Due to the above described physical system parameters, the widespread resonating double negative resonator induces a frequency-dependent shear force in the metabeam, which always changes the shear force boundary condition.

Moreover, all the continuity conditions can be non-dimensionalized using the assumed displacement as done for Eq. (3). Therefore, all the continuity conditions in Eq. (4) can be condensed in the form of a matrix, as given below

$$\begin{aligned} &\underbrace{\begin{bmatrix} 1 & 0 & 1 & 0 \\ 0 & \lambda & 0 & \lambda \\ \lambda^2 & 0 & \lambda^2 & 0 \\ \vartheta & \lambda^3 & \vartheta & \lambda^3 \end{bmatrix}}_{K} \underbrace{\begin{Bmatrix} A_n \\ B_n \\ C_n \\ D_n \end{Bmatrix}}_{\Lambda_n} = \\ &\underbrace{\begin{bmatrix} \cos\lambda & \sin\lambda & \cosh\lambda & \sinh\lambda \\ -\lambda\sin\lambda & \lambda\cos\lambda & \lambda\sinh\lambda & \lambda\cosh\lambda \\ -\lambda^2\cos\lambda & -\lambda^2\sin\lambda & \lambda^2\cosh\lambda & \lambda^2\sinh\lambda \\ \lambda^3\sin\lambda & \lambda^3\cos\lambda & \lambda^3\sinh\lambda & \lambda^3\cosh\lambda \end{bmatrix}}_{H} \underbrace{\begin{Bmatrix} A_{n-1} \\ B_{n-1} \\ C_{n-1} \\ D_{n-1} \end{Bmatrix}}_{\Lambda_{n-1}} \end{aligned} \tag{7}$$

From Eq. (7), the obtained matrices can be written as $\boldsymbol{\Lambda}_n = \mathbf{K}^{-1}\mathbf{H}\boldsymbol{\Lambda}_{n-1}$. As the proposed system is periodic, hence from the Bloch–Floquet's theorem, we can have relationship between the state vectors of the successive unit cell [6], which states

$$\boldsymbol{\phi}_n(1) = e^{-i\mu} \cdot \mathbf{I} \cdot \boldsymbol{\phi}_{n-1}(1) \tag{8}$$

where I is an identity matrix of size 4×4, ϕ is the state vector and μ is non-dimensional wave number. Therefore using Eq. (8), we can relate the state vectors in consecutive unit cells

$$\begin{aligned} &\boldsymbol{\phi}_n(1) = \mathbf{H}\boldsymbol{\Lambda}_n = \mathbf{H}\mathbf{K}^{-1}\mathbf{H}\boldsymbol{\Lambda}_{n-1} = \underbrace{\mathbf{H}\mathbf{K}^{-1}}_{T}\boldsymbol{\phi}_{n-1}(1) \\ &\rightarrow |\mathbf{T} - e^{-i\mu} \cdot \mathbf{I}|\boldsymbol{\phi}_{n-1}(1) = 0 \rightarrow e^{-i\mu} = \underbrace{\mathrm{eig}(\mathbf{T})}_{u} \\ &\rightarrow \mu = i\ln(u) \end{aligned} \tag{9}$$

From the above explained methodology, the band structure of double negative metabeam can be obtained for a unit cell using the transfer matrix method followed by the implementation of Bloch–Floquet's theorem. Here, the wavenumber is a logarithmic function of the eigenvalues of the transfer matrix T. The following section illustrates the band structure characteristic of the double negative metabeam.

4. Results and discussions

For simulations done in this section parameters of the beam taken are: area $A = 7.85 \times 10^{-5}$ m^2, inertia $I = 4.90 \times 10^{-10}$ m^4, length $L_b = 5 \times 10^{-2}$ m, density $\rho = 7800$ kg/m^3, Young's Modulus

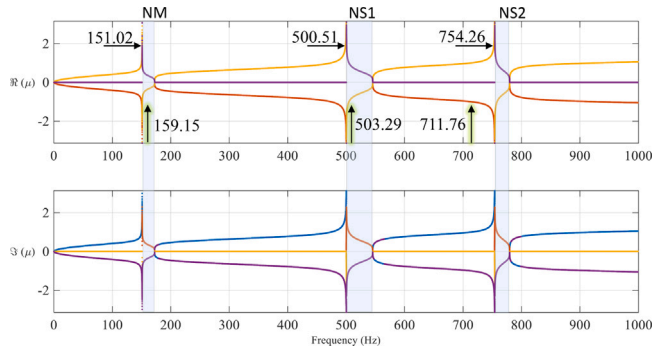

Fig. 5. Band structure of the double-negative metabeam is shown for the real and imaginary parts of the wavenumber with the excitation frequency. The attenuation bands due to the double negative resonator are highlighted. The eigenfrequencies of the 3-dof double negative resonator are marked as 151.02 Hz, 500.51 Hz, and 754.26 Hz, which are the opening frequencies of the locally resonant bandgaps. The individual natural frequencies of the resonators are marked as 159.15 Hz, 503.29 Hz, and 711.76 Hz.

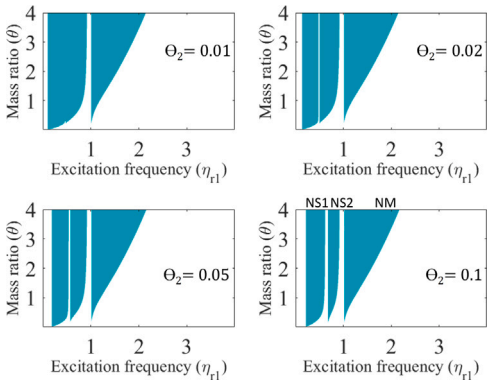

Fig. 6. Visualization of the location of various locally resonant bandgaps due to the attached 3-dof double negative resonator to the host beam. Green and white colors, respectively, show the attenuation and propagation bands. The band structure subplots are shown between the of mass ratio θ and resonating excitation frequency ratio η_{r1}. The value of mass ratio Θ_2 is defined in each subplot in the range from 0.01 to 0.1 and the mass ratio $\Theta_1 = 0.1$. (For interpretation of the references to color in this figure legend, the reader is referred to the web version of this article.)

$E = 2.1 \times 10^{11}$ N/m^2, natural frequency $f_b = 825.70$ Hz. For the local resonator vertical and horizontal dimensions are $L = 0.01$ m and $D = 0.02$ m , respectively. The stiffness of springs are $k_1 = 1 \times 10^5$ N/m, $k_2 = 1 \times 10^4$ N/m, and $k = 1 \times 10^5$ N/m, masses attached are having values $m_1 = 5 \times 10^{-3}$ kg, $m_2 = 1 \times 10^{-2}$ kg and $m = 1 \times 10^{-2}$ kg.

Fig. 5 describes the complex band structure of the double negative metabeam. The imaginary and real parts of the wavenumber (μ) are shown on the y-axis for attenuation and propagation band identification. On the x-axis, the excitation frequency is represented in Hz. Total three attenuation bands can be observed on the frequency spectrum in the frequency ranges 151.0–172.50 Hz, 500.10–545.50 Hz, and 754.20–780.70 Hz. It implies the formation of three attenuation bands, namely negative mass attenuation band (NM) and two negative stiffness attenuation bands (NS1 and NS2), as per the natural frequencies of the respective individual resonators. The individual natural frequencies of the resonators are marked as 159.15 Hz, 503.29 Hz, and 711.76 Hz in Fig. 5. The resonators having natural frequencies 503.29 Hz and 711.76 Hz contribute to the formation of negative stiffness bandgaps (NS1 and NS2). On the other side, the resonator having a natural frequency of 159.15 Hz helps in the formation of a negative mass bandgap (NM). The negative stiffness attenuation bands NS1 and NS2 are in the frequency range 500.10–545.50 Hz and 754.20–780.70 Hz, respectively, whereas the negative mass attenuation band NM is exhibited in the region 151.0–172.50 Hz. The bandgap due to the negative mass resonator is observed before the bandgaps associated with negative stiffness.

The natural frequency of the negative stiffness resonator is not situated in the negative stiffness bandgap NS2. Due to multi-degree of freedom resonator, there is a shift in the natural frequency of the double negative resonator. The natural frequencies of all individual resonators will not fall independently in bandgaps. For this, we need to calculate the eigenfrequencies of the 3-dof double negative resonator with the help of mass and stiffness matrix as reported in Appendix B. The eigenfrequencies are highlighted in Fig. 5 and having values 151.02 Hz, 500.51 Hz, and 754.26 Hz. These eigenfrequencies are present at the lower edging frequencies of the negative stiffness (NS1 and NS2) and negative mass (NM) bandgaps. These are the opening frequencies for the locally resonant bandgaps.

4.1. Merging of the attenuation bands

This section addresses merging of the negative stiffness and mass-controlled locally resonant attenuation bandgaps on the frequency spectrum for wideband vibration control. For this, the identification of critical system parameters is essential. The parameters η_{r1}, θ, Θ_1, Θ_2, κ_1, κ_2 and μ_s derived in Section 3 are used to get the bandstructure of the double negative metabeam in the non-dimensional domain. Tuning these system parameters can yield an enlarged attenuation band due to merging of negative stiffness bandgaps with the negative mass bandgap. In Figs. 6, 7, 8 and 9, in each subplot on x and y-axis, resonating frequency ratio η_{r1} and the mass ratio θ are shown, respectively. θ ranges from 0.1 to 4 in all simulations to study the effect on the width of the locally resonant bandgaps. However, in practice, the mass ratio of the resonator and beam unit cell should not be greater than 1. Fig. 6 illustrates the location of different locally resonant bandgaps due to the negative stiffness and mass resonators on the frequency axis. Here, the two negative stiffness-controlled bandgaps are merged. The specific value of the mass ratio Θ_2 is defined in the range from 0.01 to 0.1 in each subplot, whereas the mass ratio $\Theta_1 = 0.1$ is fixed. Hence, the first two locally resonant bandgaps are associated with negative stiffness resonators, and the third bandgap is because of the negative mass resonator. The negative mass controlled bandgap (NM) width is constant throughout due to the fixed value of $\Theta_1 = 0.1$. As explicated in Fig. 5, the three locally resonant bandgaps are again delineated here. The width of locally resonant bands increases with θ in all the subplots. For $\Theta_2 = 0.01$, the two bandgaps NS1 and NS2 associated with negative stiffness resonator can be perceived together, resulting in a wider attenuation band. For increasing Θ_2, the negative stiffness bandgap NS2 moves far from the NS1 bandgap. To obtain the maximum width of the attenuation band, the two merged bandgaps must be placed adjacent. In the case of merging, there may be a possibility of no bandgap or reduced attenuation band. It is also essential to comprehend the attenuation level in these locally resonant bandgaps.

Fig. 7 elucidates the level of attenuation in the merged negative stiffness controlled bandgaps. The black contour lines in each subplot exhibit a high attenuation level in a particular locally resonant bandgap, whereas the yellow contour lines show a low attenuation level. In the case of $\Theta_2 = 0.01$, the attenuation level is low compared to the $\Theta_2 = 0.02$ and $\Theta_2 = 0.05$, hence with increasing width of the attenuation band due to the merging, the level of attenuation decreases.

Fig. 8 describes the merging of negative stiffness and mass-controlled bandgaps on the frequency spectra. A specific value of the mass ratio Θ_1 is defined in the range from 0.6 to 2.0 in each subplot, whereas the mass ratio $\Theta_2 = 0.05$ is constant in each subplot. Hence, due to assumed values of Θ_1 and Θ_2, the first two locally resonant bandgaps belong to the negative stiffness resonators, and the third bandgap is associated with the negative mass resonators. The negative stiffness-controlled

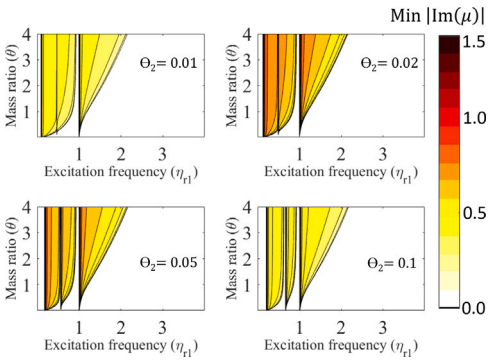

Fig. 7. Visualization of attenuation level in various locally resonant bandgaps due to the attached 3-dof double negative resonator to the host beam. The yellow color exhibits the low attenuation level and the black color high attenuation level in various locally resonant bandgaps. The attenuation level in each subplot are shown between the of mass ratio θ and resonating excitation frequency ratio η_{r1}. The value of mass ratio Θ_2 is defined in each subplot in the range from 0.01 to 0.1 and the mass ratio $\Theta_1 = 0.1$. (For interpretation of the references to color in this figure legend, the reader is referred to the web version of this article.)

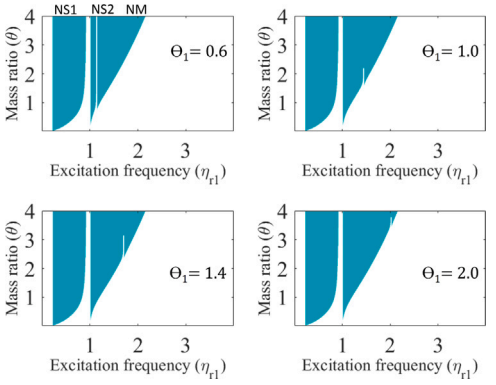

Fig. 8. Visualization of the location of various locally resonant bandgaps due to the attached 3-dof double negative resonator to the host beam. Green and white colors, respectively, show the attenuation and propagation bands. The band structure subplots are shown between the of mass ratio θ and resonating excitation frequency ratio η_{r1}. The value of mass ratio Θ_1 is defined in each subplot in the range from 0.6 to 2.0 and the mass ratio $\Theta_2 = 0.05$. (For interpretation of the references to color in this figure legend, the reader is referred to the web version of this article.)

bandgap (NS1) width is constant throughout due to a fixed value of Θ_2. It implies NS1 is due to the spring–mass system (m, k) in the negative stiffness resonator. For $\Theta_1 = 0.1$, we can observe the two adjacent bandgaps, NS2 and NM, leading to the enlarged attenuation bandgap. These two bandgaps are entirely adjacent to each other after $\theta = 2.0$. Further increasing the value of Θ_1 reduces the width of attenuation band NM and is merged with NS2 for a higher value of θ close to 4.0.

Fig. 9 explicates the level of attenuation in the merged negative stiffness and mass controlled bandgaps. In the case of $\Theta_1 = 0.6$, the level of attenuation is low as compared to $\Theta_1 = 1.0$. Here, the bands NS2 and NM1 come closer to increase the attenuation level, and further in the subsequent subplots, the separation decreases along with the attenuation level.

Table 1 shows the increase in average bandwidth after merging the NS1 and NS2 attenuation bands. A substantial increase of 164% is observed in the attenuation bandwidth, when NS1 and NS2 are adjacent. Likewise, Table 2 explains the average bandwidth after merging the NS2 and NM attenuation bands. Here, after getting perfectly adjacent to each other, the merging of both NS2 and NM produces an increase of 72.73% in the attenuation bandwidth.

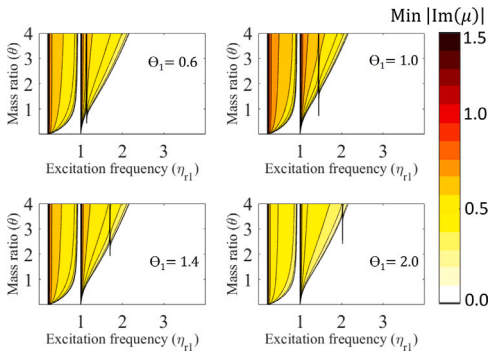

Fig. 9. Visualization of attenuation level in various locally resonant bandgaps due to the attached 3-dof double negative resonator to the host beam. The yellow color exhibits the low attenuation level and the black color high attenuation level in various locally resonant bandgaps. The attenuation level in each subplot are shown between the of mass ratio θ and resonating excitation frequency ratio η_{r1}. The value of mass ratio Θ_1 is defined in each subplot in the range from 0.6 to 2.0 and the mass ratio $\Theta_2 = 0.05$. (For interpretation of the references to color in this figure legend, the reader is referred to the web version of this article.)

Table 1
Merging of NS1 and NS2.

Bandgap	$[\eta_{r1}]_l$	$[\eta_{r1}]_u$	ABW (%)
NS1	0.206	0.626	29.6
NS2	0.676	0.911	101
NS1+NS2	0.091	0.926	164.2

Table 2
Merging of NS2 and NM.

Bandgap	$[\eta_{r1}]_l$	$[\eta_{r1}]_u$	ABW (%)
NS2	1.006	1.126	11.25
NM	1.146	2.146	60.75
NS2+NM	1.006	2.156	72.73

where $ABW = \frac{[\eta_{r1}]_u - [\eta_{r1}]_l}{\left\{\frac{[\eta_{r1}]_u + [\eta_{r1}]_l}{2}\right\}}$, which is the normalized arithmetic mean based attenuation bandwidth.

5. Conclusions and future work

Locally resonant bandgaps for an elastic beam attached with periodic 3-dof double negative resonator have been investigated analytically. A generalized form of the transfer matrix method in conjunction with the Bloch–Floquet theorem has been derived to obtain the band structure of the double negative metabeam. Due to the attached special 3-dof double negative resonator to the host beam, two negative stiffness (NS1 and NS2) and one negative mass (NM) controlled locally resonant bandgaps are observed on the frequency spectrum. These bandgaps start with a lower edging frequency, which is the eigenfrequency of the 3-dof double negative resonator. The locally resonant bandgaps formed due to the negative stiffness and mass properties of the mechanical metamaterials are merged to obtain an elongated attenuation band for wider band vibration control. Two negative stiffness (NS1 and NS2) controlled resonant bandgaps are found to be merging for the mass ratio $\Theta_2 = 0.01$. Negative stiffness (NS2) and negative mass (NM2) controlled resonant bandgaps merge for the mass ratio $\Theta_1 > 1.0$ but extent of merging shifts to higher mass ratio θ for increased Θ_1. A substantial increase of 164% is observed in the attenuation bandwidth due to merging the two negative stiffness-controlled resonant bandgaps.

A possible extension of this study could be the double negative curved metabeam, which can be applied in ring-type metastructures [28]. Periodicity can be perceived by having repeated variations of the boundary conditions. The effect of elastic support and buckling constraints should also be considered in unit cells [29].

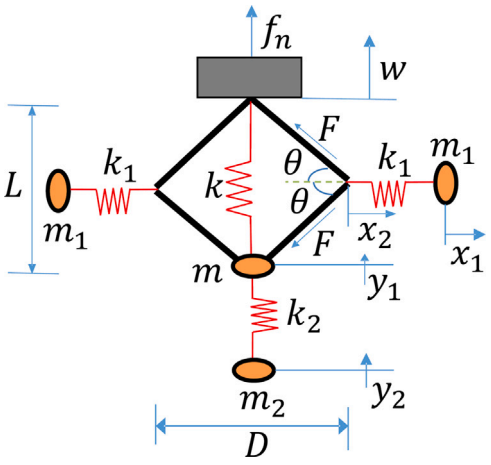

Fig. A.10. Free body diagram of the double negative local resonator.

Declaration of competing interest

The authors declare that they have no known competing financial interests or personal relationships that could have appeared to influence the work reported in this paper.

Acknowledgments

The authors like to acknowledge Visvesvaraya Ph.D. Scheme, Media Lab Asia, Ministry of Electronics and Information Technology, Government of India, for supporting the scholarship (MEITY-PHD-891) of A.D. The authors also would like to acknowledge the SPARC project (MHRD/ME/2018544) for supporting this work.

Appendix A. Shear force on the metabeam unit cell due to the attached 3-dof double negative resonator

Equations of motion the entire system can be written as

$$m_1\ddot{x}_1 + k_1(x_1 - x_2) = 0 \tag{A.1}$$

$$m_2\ddot{y}_2 + k_2(y_2 - y_1) = 0 \tag{A.2}$$

$$2F\cos\theta = k_1(x_1 - x_2) \tag{A.3}$$

$$m\ddot{y}_1 + k(y_1 - w) + k_2(y_1 - y_2) + \frac{L}{D}k_1(x_1 - x_2) = 0 \tag{A.4}$$

$$2F\sin\theta = f_n + k(w - y_1) \tag{A.5}$$

where x, y, and w are displacements and f_n is the shear force introduced in the metabeam due to the attached 3-dof double negative resonator. F is the internal force-induced inside the bars. θ is the half-angle between the bars (see Fig. A.10). Eqs. (A.3) and (A.5) give

$$f_n = k_1(x_1 - x_2)\tan\theta + k(y_1 - w) \tag{A.6}$$

where $\tan\theta = \alpha = \frac{L}{D}$ is the aspect ratio of the 3-dof double negative resonator.

From the basic kinematics, relation between displacements can be written

$$x_2 = -\frac{L}{2D}[y_1 - w] \tag{A.7}$$

From Eqs. (A.1), (A.2) and (A.5) we can write the displacements x_1, y_2 and y_1 respectively as

$$x_1 = \frac{k_1 x_2}{k_1 - m_1\overline{\omega}^2} \tag{A.8}$$

$$y_2 = \frac{k_2 y_1}{k_2 - m_2\overline{\omega}^2} \tag{A.9}$$

$$y_1 = \frac{kw + k_2 y_2 - \alpha k_1(x_1 - x_2)}{k + k_2 - m\overline{\omega}^2} \tag{A.10}$$

Now with help of Eqs. (A.7)–(A.9), displacement y_1 can be written as function of displacement w introduced in the metabeam due to the 3-dof double negative resonator

$$y_1 = \frac{\left[k - \frac{\alpha^2 k_1}{2}\frac{m_1\overline{\omega}^2}{\left(k_1 - m_1\overline{\omega}^2\right)}\right]w}{\left[\left(k - m\overline{\omega}^2\right) - \frac{k_2 m_2\overline{\omega}^2}{\left(k_2 - m_2\overline{\omega}^2\right)} - \frac{\alpha^2 k_1}{2}\frac{m_1\overline{\omega}^2}{\left(k_1 - m_1\overline{\omega}^2\right)}\right]} \tag{A.11}$$

From Eq. (A.6), using Eqs. (A.7), (A.8) and (A.11), the shear force f_n can be rewritten with non-dimensionalized terms as the function of displacement w

$$f_n = wk_1\left[\frac{\alpha^2}{2}\frac{\overline{\Omega}^2}{{\Omega_1}^2 - \overline{\Omega}^2} - \frac{1}{\kappa_1}\right]\left[1 - \frac{1}{1 - \frac{\left\{\kappa_2\frac{\overline{\Omega}^2}{{\Omega_2}^2 - \overline{\Omega}^2} + \frac{\overline{\Omega}^2}{{\Omega_3}^2}\right\}}{\left\{1 - \kappa_1\frac{\alpha^2}{2}\frac{\overline{\Omega}^2}{{\Omega_1}^2 - \overline{\Omega}^2}\right\}}}\right] \tag{A.12}$$

where the non-dimensionalized parameters $\kappa_1 = \frac{k_1}{k}$, $\kappa_2 = \frac{k_2}{k}$, $\overline{\Omega} = \frac{\overline{\omega}}{\omega}$, $\Omega_1 = \frac{\omega_1}{\omega}$, $\Omega_2 = \frac{\omega_2}{\omega}$ and $\Omega_3 = \frac{\omega_3}{\omega}$.

The effective dynamic properties (E_{eff}) of the system can be derived from the equation mentioned below after substituting the closed-form expressions of y_2 and y_1 given in Eqs. (A.9) and (A.11), respectively.

$$E_{eff} = m\dot{y}_1 + m_2\dot{y}_2 \tag{A.13}$$

Appendix B. Eigenfrequencies of the 3-dof double negative resonator

Eqs. (A.8)–(A.10) can be rewritten as

$$\left(k_1 - m_1\overline{\omega}^2\right)x_1 - k_1 x_2 = 0 \tag{B.1}$$

$$\left(k_2 - m_2\overline{\omega}^2\right)y_2 - k_2 y_1 = 0 \tag{B.2}$$

$$\left(k + k_2 - m\overline{\omega}^2\right)y_1 - kw - k_2 y_2 + \alpha k_1(x_1 - x_2) = 0 \tag{B.3}$$

Using Eq. (A.7), x_2 can be eliminated from Eqs. (B.1)–(B.3) and all three equations can be condensed in form a matrix as

$$\begin{bmatrix} \left(k_1 - m_1\overline{\omega}^2\right) & 0.5k_1\alpha & 0 \\ k_1\alpha & \left(k + k_2 + 0.5k_1\alpha^2 - m\overline{\omega}^2\right) & -k_2 \\ 0 & -k_2 & \left(k_2 - m_2\overline{\omega}^2\right) \end{bmatrix}\begin{Bmatrix} x_1 \\ y_1 \\ y_2 \end{Bmatrix} = \begin{Bmatrix} 0 \\ 0 \\ 0 \end{Bmatrix} \tag{B.4}$$

By substituting the quantitative values of the system parameters stated in Section 4, the matrix given in Eq. (B.4) can be solved for all the eigenfrequencies of the 3-dof double negative resonator and can be found as $\overline{\omega}$ = 151.02 Hz, 500.51 Hz, 754.26 Hz.

References

[1] A.F. Russillo, G. Failla, F. Fraternali, Free and forced vibrations of damped locally-resonant sandwich beams, Eur. J. Mech. A Solids 86 (2021) 104188.

[2] A. Singh, A. Banerjee, B. Bhattacharya, Waves in elastically coupled sandwich beams: An analytical investigation, Mech. Res. Commun. (2021) 103736.

[3] L. Liu, M.I. Hussein, Wave motion in periodic flexural beams and characterization of the transition between bragg scattering and local resonance, J. Appl. Mech. 79 (1) (2012).

[4] Y. Xiao, J. Wen, D. Yu, X. Wen, Flexural wave propagation in beams with periodically attached vibration absorbers: band-gap behavior and band formation mechanisms, J. Sound Vib. 332 (4) (2013) 867–893.

[5] V. Gupta, S. Adhikari, B. Bhattacharya, Exploring the dynamics of hourglass shaped lattice metastructures, Sci. Rep. 10 (1) (2020) 1–12.

[6] D. Yu, Y. Liu, G. Wang, H. Zhao, J. Qiu, Flexural vibration band gaps in timoshenko beams with locally resonant structures, J. Appl. Phys. 100 (12) (2006) 124901.

[7] M.Y. Wang, X. Wang, Frequency band structure of locally resonant periodic flexural beams suspended with force–moment resonators, J. Phys. D: Appl. Phys. 46 (25) (2013) 255502.

[8] G. Hu, L. Tang, R. Das, Internally coupled metamaterial beam for simultaneous vibration suppression and low frequency energy harvesting, J. Appl. Phys. 123 (5) (2018) 055107.

[9] A. Dwivedi, A. Banerjee, B. Bhattacharya, Study of piezo embedded negative mass metamaterial using generalized Bloch theorem for energy harvesting system, in: Active and Passive Smart Structures and Integrated Systems XIII, vol. 10967, SPIE, 2019, pp. 656–666.

[10] S. Hao, Z. Wu, F. Li, C. Zhang, Enhancement of the band-gap characteristics in disordered elastic metamaterial multi-span beams: Theory and experiment, Mech. Res. Commun. 113 (2021) 103692.

[11] Y. Xiao, J. Wen, G. Wang, X. Wen, Theoretical and experimental study of locally resonant and bragg band gaps in flexural beams carrying periodic arrays of beam-like resonators, J. Vib. Acoust. 135 (4) (2013).

[12] F. Pires, C. Claeys, E. Deckers, W. Desmet, The impact of resonant additions' footprint on the stop band behavior of 1D locally resonant metamaterial realizations, J. Sound Vib. 491 (2021) 115705.

[13] G. Hu, A.C. Austin, V. Sorokin, L. Tang, Metamaterial beam with graded local resonators for broadband vibration suppression, Mech. Syst. Signal Process. 146 (2021) 106982.

[14] T. Wang, M.-P. Sheng, Q.-H. Qin, Multi-flexural band gaps in an Euler–Bernoulli beam with lateral local resonators, Phys. Lett. A 380 (4) (2016) 525–529.

[15] G. Failla, R. Santoro, A. Burlon, A.F. Russillo, An exact approach to the dynamics of locally-resonant beams, Mech. Res. Commun. 103 (2020) 103460.

[16] H. Huang, C. Sun, G. Huang, On the negative effective mass density in acoustic metamaterials, Internat. J. Engrg. Sci. 47 (4) (2009) 610–617.

[17] S. Pope, H. Laalej, A multi-layer active elastic metamaterial with tuneable and simultaneously negative mass and stiffness, Smart Mater. Struct. 23 (7) (2014) 075020.

[18] T.A. Hewage, K.L. Alderson, A. Alderson, F. Scarpa, Double-negative mechanical metamaterials displaying simultaneous negative stiffness and negative Poisson's ratio properties, Adv. Mater. 28 (46) (2016) 10323–10332.

[19] E. Ghavanloo, S.A. Fazelzadeh, H. Rafii-Tabar, Formulation of an efficient continuum mechanics-based model to study wave propagation in one-dimensional diatomic lattices, Mech. Res. Commun. 103 (2020) 103467.

[20] H.-H. Huang, C.-T. Sun, Anomalous wave propagation in a one-dimensional acoustic metamaterial having simultaneously negative mass density and Young's modulus, J. Acoust. Soc. Am. 132 (4) (2012) 2887–2895.

[21] A. Dwivedi, A. Banerjee, B. Bhattacharya, Simultaneous energy harvesting and vibration attenuation in piezo-embedded negative stiffness metamaterial, J. Intell. Mater. Syst. Struct. (2020).

[22] B. Banerjee, An Introduction to Metamaterials and Waves in Composites, Crc Press, 2011.

[23] H. Huang, C. Sun, Theoretical investigation of the behavior of an acoustic metamaterial with extreme Young's modulus, J. Mech. Phys. Solids 59 (10) (2011) 2070–2081.

[24] H. Huang, C. Sun, Wave attenuation mechanism in an acoustic metamaterial with negative effective mass density, New J. Phys. 11 (1) (2009) 013003.

[25] A. Dwivedi, A. Banerjee, S. Adhikari, B. Bhattacharya, Optimal electromechanical bandgaps in piezo-embedded mechanical metamaterials, Int. J. Mech. Mater. Des. 17 (2) (2021) 419–439.

[26] A. Dwivedi, A. Banerjee, B. Bhattacharya, A novel approach for maximization of attenuation bandwidth of the piezo-embedded negative stiffness metamaterial, in: Active and Passive Smart Structures and Integrated Systems XIV, vol. 11376, International Society for Optics and Photonics, 2020, p. 113762F.

[27] A. Dwivedi, A. Banerjee, B. Bhattacharya, Dynamics of piezo-embedded negative stiffness mechanical metamaterials: A study on electromechanical bandgaps, in: ASME International Mechanical Engineering Congress and Exposition, vol. 84478, American Society of Mechanical Engineers, 2020, V001T01A015.

[28] F. Fraternali, G. Bilotti, Nonlinear elastic stress analysis in curved composite beams, Comput. Struct. 62 (5) (1997) 837–859.

[29] F. Fraternali, S. Spadea, L. Ascione, Buckling behavior of curved composite beams with different elastic response in tension and compression, Compos. Struct. 100 (2013) 280–289.